International Journal of Thermal Sciences 53 (2012) 188–201

Contents lists available at SciVerse ScienceDirect

International Journal of Thermal Sciences

journal homepage: www.elsevier.com/locate/ijts

Power transformer thermal analysis by using an advanced coupled 3D heat transfer and fluid flow FEM model

Marina A. Tsili [a,*], Eleftherios I. Amoiralis [b], Antonios G. Kladas [a], Athanassios T. Souflaris [c]

[a] Faculty of Electrical & Computer Engineering, National Technical University of Athens, GR-15780 Athens, Greece
[b] Department of Production Engineering and Management, Technical University of Crete, Chania 73100, Greece
[c] Schneider Electric AE, Elvim Plant, 32011 Inofyta, Greece

ARTICLE INFO

Article history:
Received 28 December 2010
Received in revised form
26 September 2011
Accepted 17 October 2011
Available online 18 November 2011

Keywords:
Power transformers
Thermal analysis
Computational fluid dynamics
Finite element method

ABSTRACT

Thermal performance in oil-immersed power transformers is governed by the flow of oil, acting both as an electrical insulator and a medium for the transfer of heat generated in the core and windings toward the tank and the surrounding air. This paper presents the development of an advanced three-dimensional (3D) finite element model for the coupled solution of heat transfer and fluid flow equations governing transformer thermal performance. The main advantages of the proposed method are: (i) no need to predefine the convection coefficients at the interfaces between the active part/tank walls and the circulating oil, (ii) detailed representation of specific transformer parts that play an important role in the accurate representation of oil flow and heat dissipation (such as winding cooling ducts and corrugated tank panels) through an automated design process, enhancing the model accuracy with the least possible computational effort and (iii) accurate definition of the transformer heat sources (core and windings loss). The proposed methodology provides an integrated tool for thermal simulation, able to predict detailed thermal distribution in a specific transformer, without requiring prior knowledge of nodal temperature or temperature gradient values.

1. Introduction

Finite element method (FEM), as well as other numerical methods, has been extensively applied in thermal analysis of electric machines and transformers, providing enhanced representation of the geometrical configuration of the considered devices, in an effort to replace semi-empirical methods involving analytical formulas and constants deriving from experimental results [1]. The finite difference method is proposed by Pierce [2] for hottest-spot temperature prediction in dry-type transformers. Two-dimensional (2D) FEM thermal calculation is proposed in Ref. [3] for the calculation of core hottest-spot temperature in power and distribution transformers. Moreover, it is employed to model the effect of harmonic currents in the winding temperature [4] and to perform heat transfer analysis and obtain the steady state and the transient temperature distribution of SF_6 gas cooled-insulated power transformers [5]. Most recent trends in thermal modeling employ coupled electromagnetic-thermal finite element models [6,7]. In Ref. [8] a 3D FEM model using a magnetic scalar potential formulation is combined with a mixed analytical and numerical form of the electrical circuit equation to take into account the skin and proximity effects in the windings, resulting to current densities that are used as inputs to FEM for the solution of steady state thermal equations. In Ref. [9] a method that relies on the combination of analytical calculations, 2D FEM for the solution of thermal equations and 3D FEM for the solution of electromagnetic equations is presented for transformer thermal modeling. Rosas et al. propose the finite volume method as a means of predicting the improvement of the cooling process of liquid-immersed electrical transformers using heat pipes [10]. However, such analysis requires correct definition of heat convection coefficient constants and boundary conditions, which are influenced by the oil flow in the transformer tank. Therefore, the application of standalone FEM for power transformer thermal calculations requires significant computational effort and experimental data for this definition. For the accurate calculation of these parameters, the coolant flow distribution must be modeled, therefore necessitating the incorporation of computational fluid dynamics (CFD) tools to the analysis. 2D coupled analysis is performed in Refs. [11] and [12]. Numerical modeling of heat transfer and fluid flow in power

* Corresponding author. Tel./fax: +30 210 7722336.
E-mail addresses: mtsili@central.ntua.gr (M.A. Tsili), eamir@tee.gr (E. I. Amoiralis), kladasel@central.ntua.gr (A.G. Kladas), thanassis.souflaris@gr.schneider-electric.com (A.T. Souflaris).

1290-0729/$ – see front matter © 2011 Elsevier Masson SAS. All rights reserved.
doi:10.1016/j.ijthermalsci.2011.10.010

Nomenclature

α_m $(m=i,j,k,l)$ coefficients used in finite element discretization
b_m $(m=i,j,k,l)$ coefficients used in finite element discretization
$[C]$ pressure gradient matrix
$[C]^T$ divergence matrix
c_m $(m=i,j,k,l)$ coefficients used in finite element discretization
c_p specific heat ($J\,kg^{-1}\,(^\circ C)^{-1}$)
d_m $(m=i,j,k,l)$ coefficients used in finite element discretization
D dimension of the physical space (2 or 3)
E thermodynamic internal energy (J)
f traction force (N)
f_n normal component of f on Γ (N)
$[F]$ vector which incorporates any traction boundary conditions on velocity
f_τ tangential component of f on Γ (N)
$[F_T]$ vector which incorporates any mixed boundary conditions on velocity and traction
$\vec{g}$ gravitational acceleration (m/s^2)
h heat transfer coefficient ($W/(m^2\,^\circ C)$)
$\bar{\bar{I}}$ unit tensor
$\vec{K}$ thermal conductivity ($W/(m\,^\circ C)$)
$[K]$ viscous matrix
$[K_T]$ thermal diffusion matrix
$[M]$ mass matrix
M nodes of finite element mesh
n direction normal to the considered surface (outward pointing unit normal vector)
N nodes of finite element mesh
$[N(u)]$ advection matrix
p pressure (N/m^2)
$[P]$ vector of pressure values at each node i of the finite element mesh
$[Q]$ vector of heat source values q_i at each node i of the finite element mesh
q heat loss per unit volume (W/m^3)
s number of iterations
$[S]$ stiffness matrix
$[S^e]$ elementary stiffness matrix
T temperature ($^\circ C$)
$[T]$ vector of temperature values T_i at each node i of the finite element mesh
$\vec{u}$ Fluid velocity (m/s)
u_n normal component of $\vec{u}$ on Γ (m/s)
u_τ tangential component of $\vec{u}$ on Γ (m/s)
$[U]$ vector of velocity values at each node i of the finite element mesh
V volume of finite element (m^3)

Greek symbols
β thermal expansion coefficient ($1/^\circ C$)
Γ piecewise smooth boundary of Ω
$\bar{\bar{\varepsilon}}$ linearized strain rate tensor
$\eta_1,\eta_2,\eta_3,\eta_4$ finite element shape functions
μ dynamic viscosity ($kg\,m^{-1}\,s^{-1}$)
ρ fluid mass density (kg/m^3)
$\bar{\bar{\sigma}}$ strain rate tensor
τ unit tangent vector on the considered surface
$\{\varphi_i\}$ piecewise-polynomial basis functions used in the finite element implementation of Navier–Stokes equations
$\{\psi_i\}$ piecewise-polynomial basis functions used in the finite element implementation of Navier–Stokes equations
Ω computational domain

transformers is proposed in Ref. [13], by means of a simplified 2D configuration, consisting of an element composed of two windings wound around a core. Coupled fluid flow and heat transfer modeling by finite volume method (FVM) in three dimensions is proposed for three-phase and single-phase dry-type transformers in Refs. [14] and [15], respectively. The coupling of 3D transformer CFD-thermal analysis is a complex task that must take into account the composite details of the active part and tank geometry as well as the interaction between thermal, oil or air velocity and electromagnetic field of the device. In Ref. [16] coupled fluid flow, heat transfer and electromagnetic numerical analysis is applied in three-phase dry-type electrical transformers, further enhancing the accuracy in the prediction of transformer temperature. In Ref. [17] 3D FVM is used for modeling of fluid flow in an encapsulated three-phase dry-type transformer and is coupled to an electric circuit model and a detailed model of the windings and core for the electromagnetic field calculations, based on FEM. Coupled 3D CFD-FEM analysis of the thermal performance in oil-immersed power transformers has not been presented in the relevant literature.

In our previous work [9], a 2D hybrid analytical-numerical technique for ONAN transformer thermal analysis was presented, able to predict thermal performance at a low computational cost for optimization purposes. The present work expands thermal analysis in three dimensions, taking into account detailed transformer geometrical parameters and coupling with fluid flow dynamics. The proposed methodology involves iterative coupling of steady state non-linear heat equations and fluid flow equations, both solved by three-dimensional finite element method. The solution uses the results of electromagnetic analysis for proper definition of the transformer heat sources. The method of choice for the solution of Navier–Stokes equations is quite dependent on the application. In our case FEM was chosen for a number of reasons, as explained in the followings. The FEM implementation is based on a variational formulation of the Navier–Stokes problem in appropriate function spaces, and determines “discrete” approximations in certain finite dimensional subspaces (“trial spaces”) consisting of piecewise-polynomial functions. By this approach the discretization inherits most of the rich structure of the continuous problem, which, on the one hand provides a high computational flexibility and on the other hand facilitates a rigorous mathematical error analysis. These are the main aspects which make the FEM increasingly attractive in CFD. Methods like FVM or spectral Galerkin method are also applicable, with specific pros and cons according to each application. Table 1 of the revised paper lists the pros and cons of each method, highlighting the reasons for the choice of FEM in our case [18]. However, it must be noted that the details are the subject of much controversial discussion concerning the pros and cons of the various methods and their variants, as well as that, this conflict is partially resolved in many cases, as the differences between the methods, particularly between FEM and FVM, often disappear on general meshes. In fact, some of the FVMs can be interpreted as variants of certain “mixed” FEMs.

The paper is organized as follows: Section 2 presents the proposed methodology details, namely the heat and fluid flow equations that need to be solved in order to describe the transformer thermal performance, as well as their coupling and solution steps. Section 3 presents the application of the method to the prediction of transformer thermal performance and the

Table 1
Comparison of FEM versus other numerical methods for the solution of Navier–Stokes equations [18].

Method	Brief description	Advantages compared to FEM	Disadvantages compared to FEM
Finite difference methods	Approximation of the Navier–Stokes equations in their "strong" form by finite differences	Easy implementation	– Problems along curved boundaries, – Difficult stability and convergence analysis, – Mesh adaptation difficulty.
Finite volume methods	Approximation of the Navier–Stokes equations as a system of (cell-wise) conservation equations	Based on "physical" conservation properties	– Problems on unstructured meshes, – Difficult stability and convergence analysis, – Only heuristic mesh adaptation.
Spectral Galerkin methods	Approximation of the Navier–Stokes equations in their variational form by a Galerkin method with "highorder" polynomial trial functions	High accuracy	– Treatment of complex domains difficult, – Mesh and order (hp)-adaptation difficult.

respective results are commented. Finally, Section 4 concludes the paper.

2. Proposed methodology

The proposed methodology combines 3D FEM solution of thermal and fluid flow equations, for the derivation of the transformer temperature distribution under different loading conditions. The coupling of fluid flow equations with heat equations is necessary in order to model the oil flow within the transformer tank. Therefore, the thermal conditions at the boundaries between the transformer active part and tank components and the cooling medium are calculated by the proposed method and there is no need to externally predefine them in the thermal finite element model.

Apart the aforementioned methodology, accurate prediction of transformer thermal performance is enhanced by:

- Detailed geometry representation of transformer active part and tank: special consideration is given to the representation of design details of particular importance to thermal analysis, such as the existence of cooling ducts in the coils and the tank corrugated panels geometry. The detailed model is derived through an automated design process, enhancing the model accuracy with the least possible computational effort.
- Accurate estimation of the transformer heat sources, i.e. the core and coils loss density, which are determined through an appropriate design methodology, involving electromagnetic analysis results [21].

2.1. Solution of heat transfer equations in solids by FEM

2.1.1. Heat transfer equations

The 3D thermal transformer analysis is governed by the following form of Poisson equation:

$$K_x \cdot \frac{\partial^2 T}{\partial x^2} + K_y \cdot \frac{\partial^2 T}{\partial y^2} + K_z \cdot \frac{\partial^2 T}{\partial z^2} = q \tag{1}$$

where T is the temperature at each point of the considered domain (°C), K_x, K_y and K_z are the materials thermal conductivities in the x-, y- and z-direction, respectively (W/(m °C)) and q is the heat source in the transformer conductors and cores (W/m^3), corresponding to the respective loss density. The above equation applies to anisotropic materials in x-, y- and z-direction (the contribution of other directions, namely xy, yx, xz, zx, yz, zy, is considered negligible). The heat source is obtained through the losses in the transformer cores (no load losses) and windings (load losses), calculated through analytical formulas according to the transformer characteristics (winding and core dimensions, winding material resistivity, core material specific loss curve). These losses are considered to be uniformly dissipated along the transformer cores and windings, respectively, deriving the loss density that is used to calculate the heat source q. Equation (1) is valid under the assumption of a steady state, as well as the assumption of a homogeneous heat conductivity K distribution.

2.1.2. Boundary conditions

The proper solution of (1) involves correct definition of the boundary conditions between the transformer active part and tank components and oil (heat convection boundary conditions). The boundary condition imposed on these surfaces is expressed by the following equation:

$$|\vec{K}| \cdot \frac{\partial T}{\partial n} + h[T - T_b] = 0 \tag{2}$$

where n is the direction normal to the surface, h is the heat transfer coefficient (W/(m^2 °C)) of the considered surface, T_b is the temperature (°C) imposed on the boundary and $|\vec{K}|$ is the thermal conductivity of the material of the considered surface (since this coefficient is dependent on the x-, y- and z-coordinates, and given that the space discretization is performed by tetrahedral elements, as explained in the next section, the coordinates of the center of each tetrahedral face of the considered surface are used for the calculation of $|K|$). Complicated thermal tests and calculations are required in order to determine the true value of h [19,20], especially in the case of the surfaces between the windings and oil circulating in the ducts. However, coupling of heat flow equations to fluid flow equations does not require prior knowledge of this coefficient, as explained in the following sections.

2.1.3. Discretization via finite element method

The considered transformer temperature field is represented by a group of finite tetrahedral elements. Therefore, a continuous physical problem is converted into a discrete problem of finite elements with unknown field values in their vertices nodes. The temperature at each point inside a tetrahedral element with vertices nodes i, j, k and l, is given by

$$T(x,y,z) = \eta_1 + \eta_2 x + \eta_3 y + \eta_4 z \tag{3}$$

where coefficients η_1, η_2, η_3 and η_4 (also known as shape functions) depend on temperatures T_i, T_j, T_k, T_l and the vertices coordinates according to the following equation:

$$\begin{aligned} T_i &= \eta_1 + \eta_2 x_i + \eta_3 y_i + \eta_4 z_i \\ T_j &= \eta_1 + \eta_2 x_j + \eta_3 y_j + \eta_4 z_j \\ T_k &= \eta_1 + \eta_2 x_k + \eta_3 y_k + \eta_4 z_k \\ T_l &= \eta_1 + \eta_2 x_l + \eta_3 y_l + \eta_4 z_l \end{aligned} \tag{4}$$

The solution of the system of equations (4) yields:

$$\begin{aligned}\eta_1 &= \frac{a_iT_i + a_jT_j + a_kT_k + a_lT_l}{6V}\\ \eta_2 &= \frac{b_iT_i + b_jT_j + b_kT_k + b_lT_l}{6V}\\ \eta_3 &= \frac{c_iT_i + c_jT_j + c_kT_k + c_lT_l}{6V}\\ \eta_4 &= \frac{d_iT_i + d_jT_j + d_kT_k + d_lT_l}{6V}\end{aligned} \tag{5}$$

where

$$V = \frac{1}{6}\begin{vmatrix}1 & 1 & 1 & 1\\ x_i & x_j & x_k & x_l\\ y_i & y_j & y_k & y_l\\ z_i & z_j & z_k & z_l\end{vmatrix},\ a_i = \begin{vmatrix}x_j & y_j & z_j\\ x_k & y_k & z_k\\ x_l & y_l & z_l\end{vmatrix},\ b_i = -\begin{vmatrix}1 & y_j & z_j\\ 1 & y_k & z_k\\ 1 & y_l & z_l\end{vmatrix},$$
$$c_i = \begin{vmatrix}x_j & 1 & z_j\\ x_k & 1 & z_k\\ x_l & 1 & z_l\end{vmatrix},\ d_i = -\begin{vmatrix}x_j & y_j & 1\\ x_k & y_k & 1\\ x_l & y_l & 1\end{vmatrix} \tag{6}$$

Combining equations (3), (4) and (6) we get the following expression for the temperature at each point of the tetrahedral element:

$$T(x,y,z) = \sum_{m=i,j,k,l}\frac{1}{6V}(\alpha_m + b_mx + c_my + d_mz)T_m \tag{7}$$

The discretized form of (1) is:

$$[S]\cdot[T] = [Q] \tag{8}$$

where $[S]$ is the stiffness matrix defined by the finite element method ($N \times N$ for a finite element mesh consisting of N nodes), $[T]$ is the unknown column vector of temperature values T_i at each node i of the finite element mesh ($N \times 1$ for a finite element mesh consisting of N nodes) and $[Q]$ is the known column vector of heat source q_i at each node i of the finite element mesh ($N \times 1$ for a finite element mesh consisting of N nodes). The elements of the stiffness matrix derive by summation of each $[S^e]$ elementary stiffness matrix corresponding to tetrahedral element e of the mesh, with:

$$S^e_{pq} = \frac{|\vec{K}|_e}{36\cdot V}(b_pb_q + c_pc_q + d_pd_q) \quad \text{for } p = i,j,k,l \text{ and } q = i,j,k,l \tag{9}$$

where $|\vec{K}|_e$ is the magnitude of the heat conductivity of the element (deriving from the K_x, K_y and K_z components of the element material thermal conductivity at the center of the tetrahedral element).

2.2. Solution of CFD equations by FEM

2.2.1. Navier–Stokes and Boussinesq equations

In solid and liquid materials, heat transfer and viscous fluid flow are governed by Navier–Stokes equations, deriving from the basic principles of conservation of momentum, mass and energy.

The conservation of momentum, mass (continuity) and energy principles are described by equations (10), (11) and (12) respectively:

$$\rho\left(\frac{\partial\vec{u}}{\partial t} + (\vec{u}\cdot\nabla)\cdot\vec{u}\right) - \nabla\cdot\bar{\bar{\sigma}} = \rho\cdot\vec{g} \tag{10}$$

$$\left(\frac{\partial\rho}{\partial t} + (\vec{u}\cdot\nabla)\cdot\rho\right) + \rho\cdot(\nabla\cdot\vec{u}) = 0 \tag{11}$$

$$\rho\left(\frac{\partial E}{\partial t} + \vec{u}\cdot\nabla E\right) - \nabla\cdot(\vec{K}\cdot\Delta T) + p\nabla\cdot\vec{u} = 0 \tag{12}$$

where ρ stands for the fluid mass density (kg/m^3), $\vec{u}$ is the fluid velocity (m/s), $\bar{\bar{\sigma}}$ is the strain rate tensor, p denotes the pressure (N/m^2), $\vec{g}$ is the gravitational acceleration (m/s^2), E is the thermodynamic internal energy (J), K is the material thermal conductivity (W/(m °C)) and T is the temperature (°C).

For Newtonian fluids[1] the strain rate tensor $\bar{\bar{\sigma}}$ is given by

$$\bar{\bar{\sigma}} = 2\mu\bar{\bar{\varepsilon}} - \frac{2}{3}\mu(\nabla\cdot\vec{u})\bar{\bar{I}} - p\bar{\bar{I}} \tag{13}$$

where μ is the dynamic viscosity (kg m^{-1} s^{-1}), $\bar{\bar{I}}$ is the unit tensor and $\bar{\bar{\varepsilon}}$ is the linearized strain rate tensor, i.e.

$$\varepsilon = \begin{bmatrix}\varepsilon_{xx} & \varepsilon_{xy} & \varepsilon_{xz}\\ \varepsilon_{yx} & \varepsilon_{yy} & \varepsilon_{yz}\\ \varepsilon_{zx} & \varepsilon_{zy} & \varepsilon_{zz}\end{bmatrix} \tag{14}$$

where each component of ε_{ij} of the above matrix is yielded by

$$\varepsilon_{ij} = \frac{1}{2}\left(\frac{\partial u_i}{\partial x_i} + \frac{\partial u_j}{\partial x_j}\right) \tag{15}$$

Using equations (5) and (6) equation (2) becomes

$$\rho\left(\frac{\partial\vec{u}}{\partial t} + (\vec{u}\cdot\nabla)\cdot\vec{u}\right) - \nabla\cdot(2\cdot\mu\cdot\bar{\bar{\varepsilon}}) + \nabla p = \rho\cdot\vec{g} \tag{16}$$

In case of an incompressible material[2] p is constant and equation (11) reduces to

$$\nabla\cdot\vec{u} = 0 \tag{17}$$

Therefore, the final form of the Navier–Stokes equations used in the CFD analysis of the paper are described by (12), (16) and (17).

The thermal flow of incompressible fluids can be represented by using the Boussinesq approximation used in the field of buoyancy-driven flow (also known as natural convection, i.e. heat transport, in which the fluid motion is not generated by any external source (like a fan) but only by density differences in the fluid occurring due to temperature gradients – this type of flow is encountered to ONAN transformers). It states that density differences are sufficiently small to be neglected, except where they appear in terms multiplied by g, the acceleration due to gravity. Thus the variation in density is neglected everywhere except in the buoyancy term. For small temperature differences between the T_o and T the variation of the fluid density between ρ_o to ρ depends linearly on temperature, through the equation:

$$\rho = \rho_o\cdot(1 - \beta\cdot(T - T_o)) \tag{18}$$

where β is the thermal expansion coefficient (1/°C), while ρ_o and T_o represent reference values of mass density (kg/m^3) and temperature (°C), respectively. Assuming that the gravitational acceleration is the only external force, then the force $\rho_o\cdot\vec{g}\cdot(1 - \beta\cdot(T - T_o))$ is caused in the fluid by temperature variations.

[1] Fluids that have a linear relationship between stress and strain rate are called Newtonian fluids. This is a property of the fluid, not the flow. Water, air and the considered transformer oil are examples of Newtonian fluids, while highly viscous fluids are examples of non-Newtonian fluids.

[2] Incompressible flow is solid or fluid flow in which the divergence of velocity is zero. This is more precisely termed isochoric flow. It is an idealization used to simplify analysis. In reality, all materials are compressible to some extent. Note that isochoric refers to flow, not the material property. This means that under certain circumstances, a compressible material can undergo (nearly) incompressible flow. However, by making the 'incompressible' assumption, one can greatly simplify the equations governing the flow of the material.

2.2.2. Initial conditions

The appropriate initial conditions for equations (12), (16) and (17) are: (1) any velocity field, $\vec{u}_o$, which is solenoidal (i.e., must satisfy equation (17)) and (2) any temperature field, T_o. Note that no initial conditions are required for pressure; the initial pressure field, p_o, is contained implicitly in equations (12) and (17), given $\vec{u}_o$ and T_o.

2.2.3. Boundary conditions

(a) Velocity

In general, the computational domain Ω is to be regarded as being bounded by a piecewise smooth boundary, Γ, along which the following boundary conditions are permissible.

$$f_n = -p + 2\cdot\mu\cdot\frac{\partial u_n}{\partial n} \tag{19}$$

$$f_\tau = \mu\cdot\left(\frac{\partial u_n}{\partial \tau}+\frac{\partial u_\tau}{\partial n}\right) \tag{20}$$

Equations (19) and (20) specify u_n or f_n and u_τ or f_τ where u_n and u_τ are the normal and tangential components of $\vec{u}$ on Γ (m/s) and f_n and f_τ are the respective components of the surface traction force (N), while n and τ are the outward pointing unit normal vector and the unit tangent vector, respectively.

(b) Temperature

The general boundary condition appropriate to equation (12) is equation (2) presented in Section 2.1.2.The special case of specified temperature may be obtained from equation (2) by letting $h \to \infty$.

(c) Pressure

No pressure boundary conditions (i.e., specified pressure along a portion of Γ) are applied, since they are inconsistent with equations (12), (16) and (17) and therefore 'illegal'.

2.2.4. Discretization via finite element method

The finite element spatial discretization of equations (12), (16) and (17) is performed by the Galerkin method via the following expansions in the basis sets $\{\varphi_i\}$ and $\{\psi_i\}$, where the piecewise-polynomial basis functions are endowed with the property that all but one are zero at a particular node, and the basis function for that node is unity; this conveniently identifies the amplitude coefficients of the expansions in the basis set with nodal values of the variables – thus,

$$\underline{u}^d(\underline{x},t) = \sum_{i=1}^{N}\underline{u}_i(t)\cdot\varphi_i(\underline{x}) \tag{21}$$

$$T^d(\underline{x},t) = \sum_{i=1}^{N}T_i(t)\cdot\varphi_i(\underline{x}) \tag{22}$$

$$P^d(\underline{x},t) = \sum_{i=1}^{M}P_i(t)\cdot\psi_i(\underline{x}) \tag{23}$$

where, in the discretized domain, there are N nodes for velocity and temperature (neglecting boundary conditions) and M nodes for pressure ($N=M$ in our case, since the same discretization is used for pressure and velocity); the superscript d indicates a finite dimensional approximation. The basis functions for pressure must be at least one order lower than those for velocity [22], otherwise the final matrix of coefficients for the discretized dependent variables will be rank deficient and the solution (especially for the pressure) will be difficult or impossible to obtain. For convenience and higher accuracy, the basis functions for temperature are taken to be the same as those for velocity.

Inserting equations (21)–(23) into the weak (Galerkin) form of equations (12), (16) and (17) (which reduces differentiability requirements – φ_i can be continuous with piecewise-discontinuous first derivatives and ψ_i can be piecewise-discontinuous), leads to the following set of ordinary differential equations (ODEs), the Galerkin FEM equations, written in a compact matrix form,

$$[M]\left[\dot{U}\right]+[[K]+[N(u)]][U]+[C][P]+\beta[M]'[T]=[F]+\beta[M]'[T]_r \tag{24}$$

$$[C]^T[U] = 0 \tag{25}$$

$$[M]'\left[\dot{T}\right]+[[K_T]+[N_T(u)]][T] = [F_T] \tag{26}$$

In equations (24)–(26) $[U]$ is a global vector of length $D\times N$ (D is the dimension of the physical space; 2 or 3) containing all nodal velocity components, $[P]$ is a global $M\times 1$ vector of nodal pressures, and $[T]$ is a global $N\times 1$ vector of nodal temperatures; $[F]$ is a global vector (length $D\times N$) which incorporates any traction boundary conditions on velocity, and $[F_T]$ is an $N\times 1$ vector which incorporates any of the 'mixed' boundary conditions of equation (20). Specified nodal values of velocity and temperature are imposed directly on the assembled system, typically by deleting the equation in question and transposing all coupling terms to the right hand side (RHS) or by replacing the equation by one with all zeros except for unity on the diagonal and placing the specified value on the RHS. $[M]$ is the $D\cdot N\times D\cdot N$ "mass" matrix, $[M]'$ is an $N\times N$ subset of $[M]$ (multiplied by the appropriate scalar), $[K]$ is the $D\cdot N\times D\cdot N$ viscous matrix, $[K_T]$ is the $N\times N$ thermal diffusion matrix, $[C]$ is the $D\cdot N\times M$ pressure gradient matrix and its transpose, $[C]^T$is the $M\times D\cdot N$ divergence matrix, $[N(u)]$ is the $D\cdot N\times D\cdot N$ non-linear advection matrix, and $[N_T(u)]$is a $D\cdot N\times N$ subset of $[N(u)]$. $[M]$, $[N(u)]$, and $[N_T(u)]$ are actually composed of blocks of smaller $(N\times N)$ matrices.

2.3. Material properties

The temperature variant physical properties of mineral oil are calculated by equations (27)–(30) [13]:

$$\rho(T) = 1098.72 - 0.712T \tag{27}$$

$$\left|\vec{K}\right|(T) = 0.1509 - 7.101e^{-5}T \tag{28}$$

$$c_p(T) = 807.163 + 3.58T \tag{29}$$

$$\mu(T) = 0.08467 - 0.0004T + 5e^{-7}T^2 \tag{30}$$

where c_p is the specific heat at constant pressure (J kg^{-1} (°C)$^{-1}$), T is the temperature (in °C) and μ is the dynamic viscosity (kg m^{-1} s^{-1}).

According to equations (27)–(30), the oil density, thermal conductivity and dynamic viscosity decrease with increasing temperature, but the specific heat at constant pressure varies in the same way as the temperature.

Temperature variation for the specific heat and heat conductivity of the core and winding materials (copper and iron, respectively) is also taken into account, expressed by equations (31)–(34), and the respective variation curves for their heat conductivity and specific heat are shown in Figs. 1 and 2, respectively. Moreover, iron

and copper mass densities are considered constant and equal to 7870 kg/m^3 and 8960 kg/m^3, respectively.

$$c_p^{iron}(T) = -2.91e^{-4}T^2 + 0.522T + 431.88 \quad (31)$$

$$c_p^{copper}(T) = -3.20e^{-4}T^2 + 0.221T + 376.98 \quad (32)$$

$$\mu^{iron}(T) = 8.64e^{-5}T^2 - 0.104T + 404.18 \quad (33)$$

$$\mu^{copper}(T) = 1.22e^{-4}T^2 - 0.128T + 83.71 \quad (34)$$

Temperature T in equations (27)–(34) is the nodal temperature value (i.e. the value at the considered node of the FEM mesh, calculated according to Section 2.1.3).

Due to the non-linear characteristics of the properties described in equations (27)–(34), equation (8) becomes non-linear. The solution of non-linear equations (8) and (24)–(26) must be iterative, as explained in the following paragraphs.

2.4. Coupled 3D CFD-FEM model

The transformer 3D FEM model is illustrated in Fig. 4, consisting of the one-fourth of its real geometry (Fig. 3), i.e. half of the transformer width and length, due to symmetry, which is taken into account by the imposition of appropriate Dirichlet as well as Neumann boundary conditions. The actual wound core transformer active part consists of the high voltage (HV) and low voltage (LV) windings of three phases and four iron cores that surround them. The model of Fig. 4 comprises two of the four iron cores, the HV and LV winding of phase a, and half of the HV and LV winding of phase b (middle HV and LV windings). The cooling ducts at the parts of the windings outside the core windows are also represented as orthogonal gaps in the winding material, enabling the circulation of oil between them.

For the derivation of the transformer thermal distribution, the thermal and fluid flow equations (8) and (24)–(26) are solved iteratively, for a prescribed loss density in the transformer core and windings, derived by the loss values of the considered design. Fig. 5 illustrates the flowchart of the proposed method, describing the coupling of the thermal and fluid flow equations. Only an initial guess for the transformer temperature and oil velocity has to be defined, providing the initial condition for the coupled FEM solver. T_o in Boussinesq equation (18) is the average temperature on the horizontal symmetry plane of the FEM model. Since the procedure involves the solution of two coupled non-linear equations, a large number of iterations would result to significant execution times. The recommended practice is to provide the user the ability to select the number of non-linear iterations (preferably small values, not exceeding the number of ten), and observe the change in solution between iteration steps, so as to select the smallest one and derive the least execution time possible. Therefore, the total number of iterations s of the coupled solver has to be defined by the user, depending on the specific transformer characteristics and its loading conditions. The above process is more cost-effective than the adoption of a general number of iterations which might possibly result to extremely large execution time which could compromise the applicability of the method in the case of 3D FEM coupled problems. The initial guess for the transformer temperature and oil velocity is used only for the first iteration step. The heat equations are solved first, deriving an initial temperature field, based on the initial values provided by the user. The non-linear equations of the heat solver are linearized. Two different linearization strategies are available, namely the Picard linearization and the Newton linearization. The iterative solver begins with the Picard iterations, and if the given convergence tolerance between two iterations is not met before the iteration count takes its maximum value, the iteration type is switched to Newton until convergence is

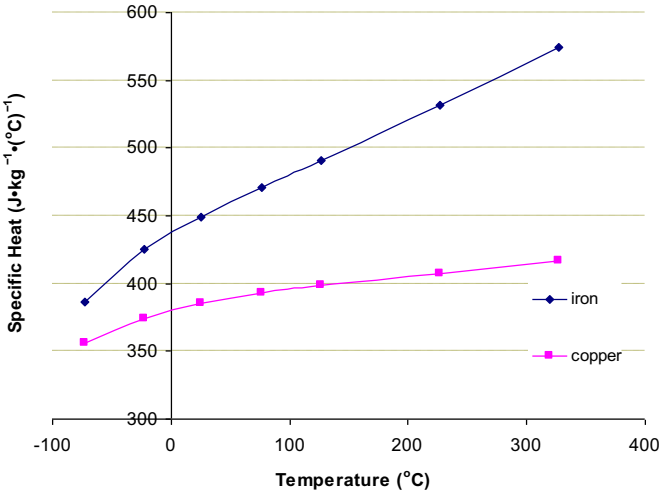

Fig. 2. Variation of iron and copper specific heat with temperature.

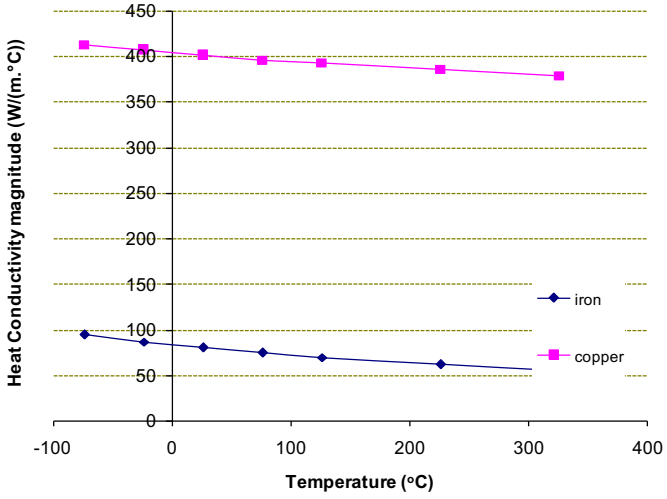

Fig. 1. Variation of iron and copper heat conductivity magnitude with temperature.

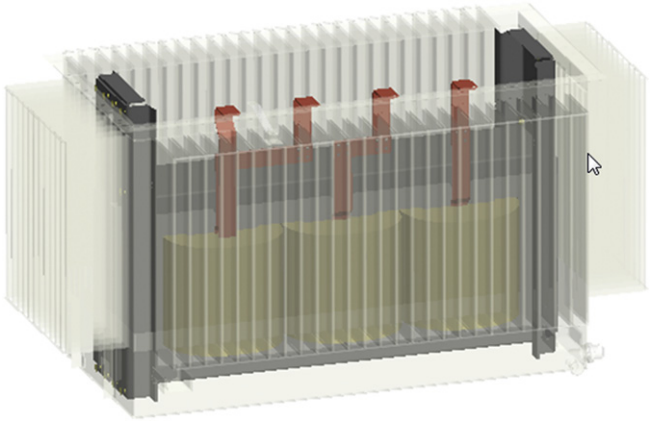

Fig. 3. Perspective view of the considered wound core distribution transformer active part and tank.

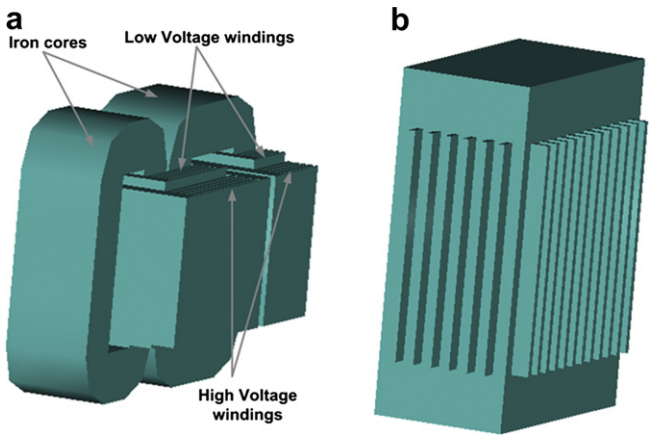

Fig. 4. Perspective view of 3D transformer FEM model: (a) active part, (b) oil tank.

achieved. If still convergence is not attained, then the solution is not feasible and the user has to redefine the initial values of temperature and oil velocity conditions. After the convergence of the heat solver, the CFD solution begins, using the temperature field values provided by the heat solver. The Picard and Newton iterations sequence is similar to the one described for the heat solver, and if convergence is not achieved initial conditions must be redefined. In order to deal with the intrinsic non-linear characteristics of the Navier–Stokes and thermal equations as well as the effect of the particular non-linear material properties involved in their solution, the FEM solver used in the methodology adopts a hybrid linearization scheme, involving two methods of linearization instead of only one. Therefore, Picard and Newton linearization methods are used successively, as they ensure complementary advantages in terms of stability and fast convergence to the solution [23]. This is the main objective for the use of hybrid Picard–Newton scheme in the diagram of Fig. 5. This process is repeated for the s iterative steps of the solution, where the temperature and oil velocity conditions computed in the $s-1$ iteration are used as initial conditions for the s iteration.

The transformer thermal limits are chosen according to the guidelines imposed by the IEEE Standard C57.91-1995 (R2002) [24]. A maximum winding and oil temperature of 120 °C and 110 °C, respectively, is imposed, based on the relative aging rate of the insulation in the transformer. These are the upper limits for the transformer windings and oil temperature and the computed transformer temperature must always be below these limits.

2.5. Heat convection calculation

The convection at the interface boundaries between the transformer active part, oil and tank is computed by the FEM solver by coupling the velocity field to the heat equation during each iteration. More specifically, according to Fig. 5, during iteration s, the non-linear heat solver calculates the thermal distribution. This distribution includes the heat fluxes and the temperature in the boundaries between the transformer active part and oil, as well as the boundaries between the tank and the oil. These data are passed to the CFD-FEM solver of s iteration and the heat convection coefficients are calculated prior to the solution process. The results of CFD-FEM of s iteration (namely, the oil velocity field) are used as input for the thermal equations solution process by FEM of the $s+1$ iteration and so on. Therefore there is no need to define convection coefficients at these boundaries. Only the initial guess of the transformer temperature and oil

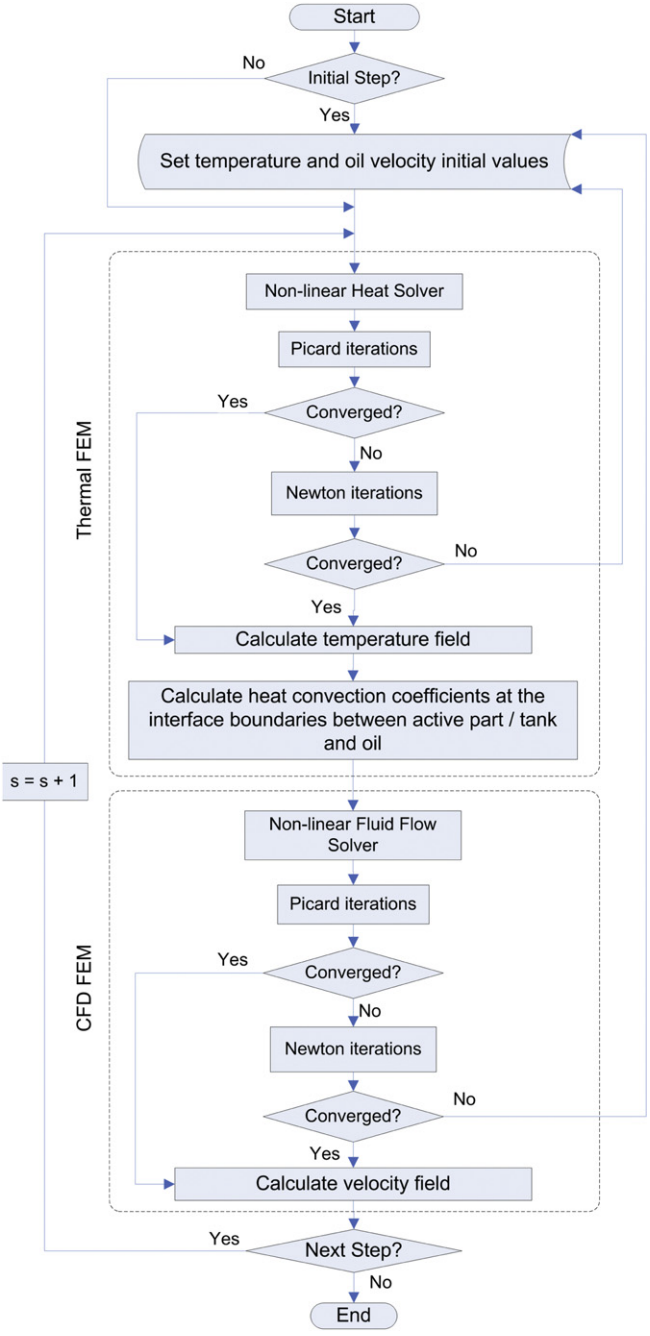

Fig. 5. Flowchart of the proposed coupled method.

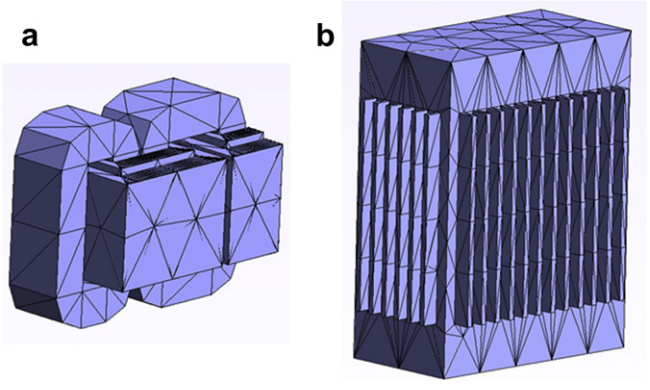

Fig. 6. Initial mesh of transformer: (a) active part and (b) oil tank.

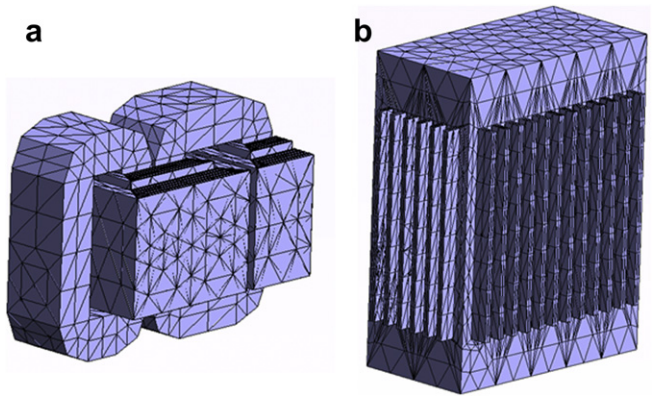

Fig. 7. Optimized mesh of transformer: (a) active part and (b) oil tank.

velocity provided by the user is used for the first time step of the solution, a guess that is not however crucial for the convergence of the method, since it is later refined by the updated results of the coupled solver. Moreover, in our case of oil cooled transformer, no radiation effects need to be taken into consideration as in the case of air-cooled ones [25].

2.6. Software implementation

The implementation of the proposed method required the development of special routines enabling the interaction of different software packages and their parameterization for the examined transformer problem. More specifically, the methodology presented in Ref. [21] was used to derive the transformer performance characteristics (losses in the transformer windings and core), based on the transformer design characteristics. The detailed model of the transformer active and mechanical part according to the design specifications was produced by the design software package presented in Ref. [26].

Next, a separate software package was employed to create and optimize the 3D FEM mesh needed for the solution of FEM equations [27]. The geometry definition for the creation of the mesh requires the construction of a 3D model with specification of coordinates of representative points of the considered geometry, taking advantage of possible existing symmetries. The pre-processing procedure concludes with discretization of the model space into finite elements. The implementation of pre-processing tasks described above can become quite complex in case of the detailed transformer geometry and requires specific computer aided design knowledge and increased effort. However, in the developed methodology, the transformer 3D geometry used as input to the meshing software was created automatically by a proper command file generated by Ref. [26] and no further user interaction was required. Fig. 6 illustrates the initial mesh created by the software, consisting of approximately 3000 nodes. As the construction of the mesh was crucial for the accuracy of the calculations conducted by the finite element method, careful consideration was given on its density and homogeneity. Meshes of various densities were constructed, providing the ability to choose the most suitable one (according to requirements in accuracy and computation time). Fig. 7 shows the active part and tank of an optimized mesh of intermediate density (equal to 12,000 nodes). The mesh of Fig. 7 derived after refinement in areas of special interest: that is why the nodes density is considerably greater in the windings area and the tank surface, in order to obtain greater accuracy in the winding ducts and tank panels region, respectively.

Finally, a finite element software (multiphysics solver Elmer) was used for the solution of the coupled problem and the post-processing of the results [28]. The CFD and heat transfer equations were implemented in the multiphysics solver (using the input of the parameterized 3D FEM transformer mesh), and were not recoded. The material properties of the active part and oil are described in Section 2.3, while the boundary conditions between the active part surfaces and the oil are given in Sections 2.1.2 and 2.2.3. The properties of the heat solver and Navier–Stokes solver are described in Fig. 5. A maximum number of eleven iterations are prescribed for each solver and the convergence tolerance is equal to $1e^{-5}$. It must be noted that while the heat flow equations are solved for the entire domain (active part and oil) the Navier–Stokes equations are solved only for the oil circulating between the active part and tank.

Special routines were implemented to obtain and visualize the solver results by interfering with the Elmer output data. This procedure was necessary in order to specialize and adapt the proposed 3D FEM method for CFD-thermal transformer modeling to the specific transformer characteristics [29], while it provides the possibility to repeat and automate the analysis involving a reduced effort.

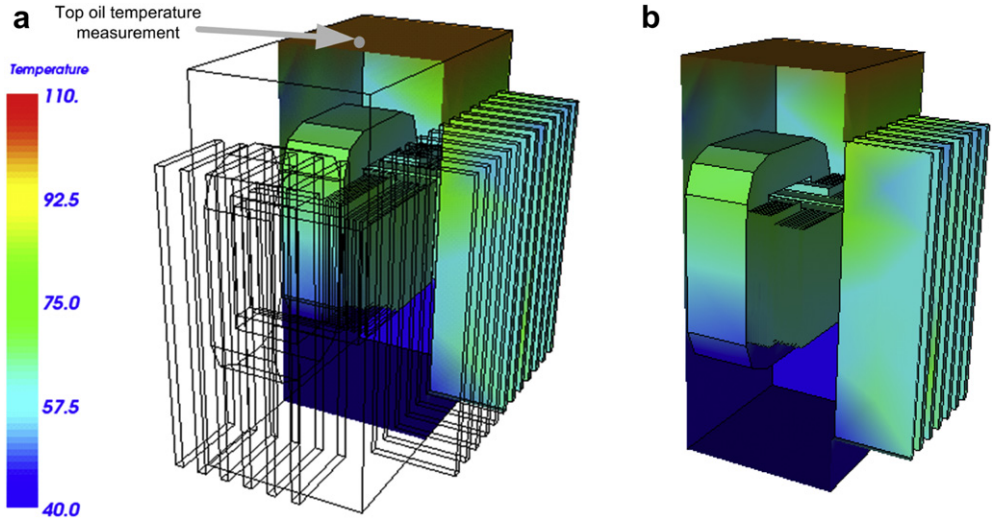

Fig. 8. Temperature distribution (in °C) at the 400 kV A transformer active part and tank walls (operation under nominal load): (a) with and (b) without wireframe tank model.

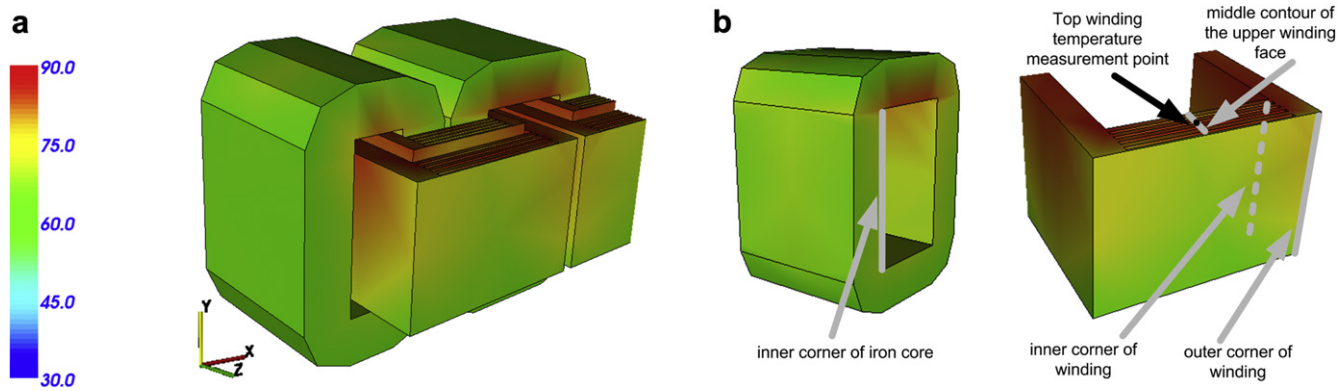

Fig. 9. Details of the temperature distribution (in °C) in the 400 kV A transformer active part (operation under nominal load): (a) entire active part, (b) core and HV winding (the center of axes in (a) corresponds to point (0,0,0) of the model geometry).

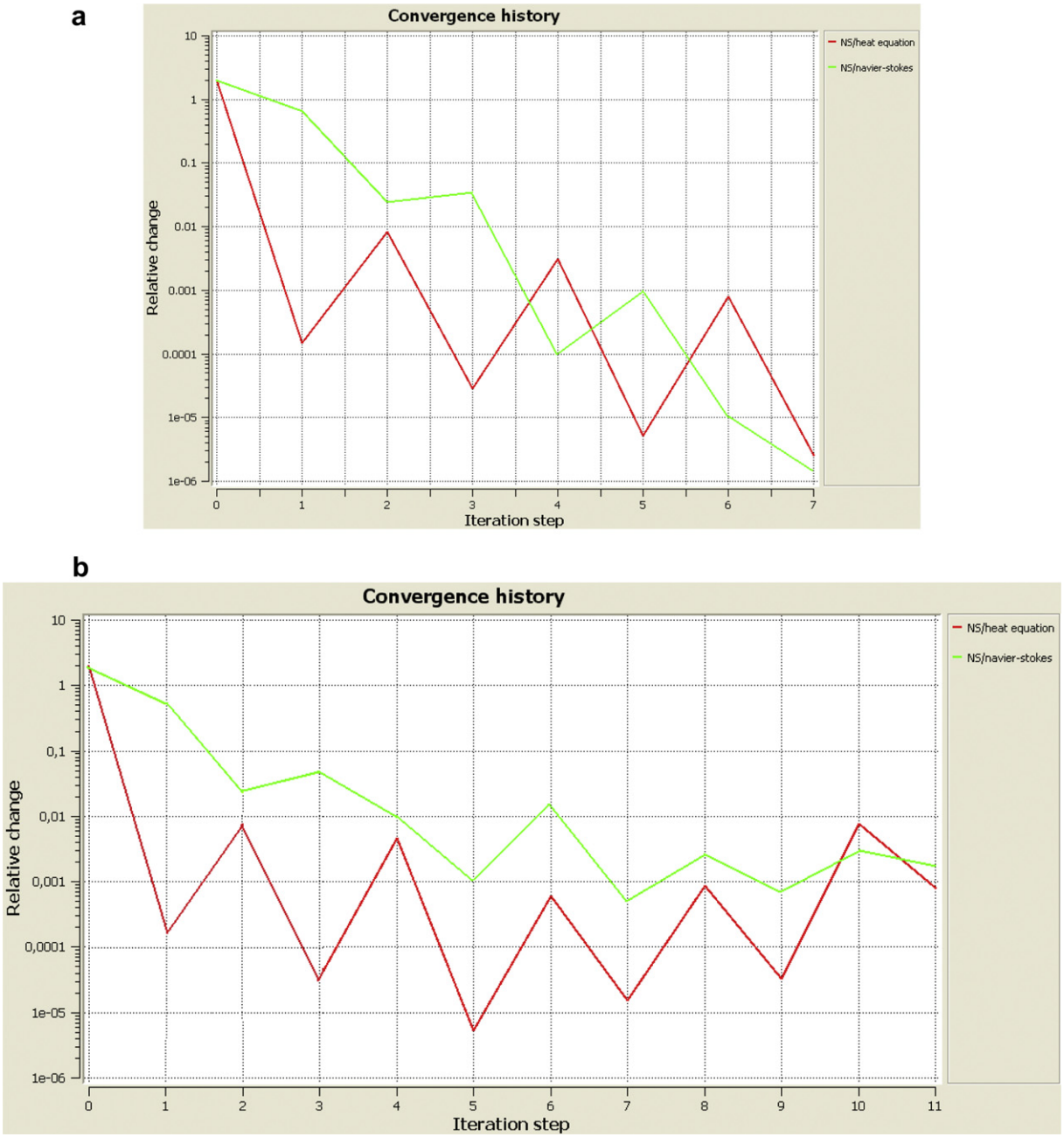

Fig. 10. Convergence characteristics of the coupled Navier–Stokes-heat non-linear solver (a) using the hybrid Picard–Newton iteration scheme and (b) using only Picard iterations.

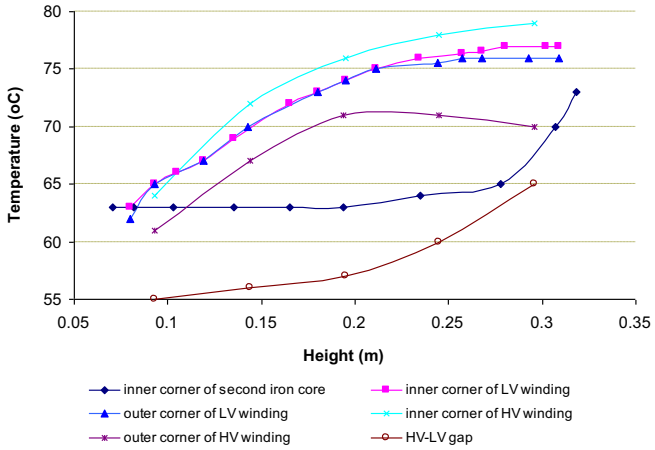

Fig. 11. Temperature variation along different vertical contours of the 400 kV A transformer core and windings (as illustrated in Fig. 9).

3. Results and discussion

The proposed method was applied for the prediction of thermal performance to transformers of different ratings, along with their comparison to the respective measured values, where available.

3.1. Application to a 400 kVA transformer

Figs. 8 and 9 illustrate the results of the method in a 400 kV A, 20–0.4 kV transformer case, operating under nominal load, at an ambient temperature equal to 30 °C. The HV windings loss is equal to 1853 W, while the LV windings loss is equal to 1554 W. All the results of this section derived with the use of the optimized mesh of Fig. 7. Fig. 8 represents the thermal distribution results inside the active part and the tank walls in half of the FEM model (the rest of the wireframe model edges are kept in the figure for better representation purposes) while Fig. 9 shows details of the results in the transformer active part. Fig. 10 shows the convergence history for the coupled Navier–Stokes heat flow solver applied in the 400 kV A transformer thermal distribution prediction. Moreover, this figure compares the convergence characteristics of the proposed hybrid Picard–Newton iteration scheme with the respective characteristics when only Picard iterations are used for each non-linear solver, illustrating the better convergence performance achieved by the hybrid scheme (in terms of relative change in the solution of each iteration and number of iterations).

Fig. 11 illustrates the variation of temperature along the contours of the active part depicted in Fig. 9. According to the curves of Fig. 11, the maximum temperature occurs at the inner corner of the HV winding, reaching the maximum value of 77 °C at the upper part of the winding. However, it must be noted that this point does not correspond to the hottest-spot of the winding, i.e. the point with the maximum winding temperature. This spot is located inside the winding, and its respective temperature is equal to 85 °C, a temperature significantly higher than the one exhibited in the outer part of the inner corner of the winding, due to the fact that this corner is in contact to the cooling medium circulating in the gap between the HV and LV winding. The variation along the contours of the inner and outer corner of LV winding, as well as the inner corner of the HV winding, exhibits similar behavior, presenting an overall gradient of approximately 15 °C. However, in the outer corner of the HV winding, where the circulation of the oil is more efficient (since no other winding is interposed between this corner and the tank walls), better cooling and heat dissipation is achieved and the temperature at the upper parts of this contour increases less than in the respective inner corner of the winding. As far as the core is concerned, the temperature rise is lower than the one in the windings, due to its lower loss density, resulting accordingly to less steep temperature gradient between its lower and upper part.

Fig. 13 illustrates the variation along the horizontal contour in the middle of the upper HV winding face of Fig. 9. In this figure, the influence of the winding ducts in the temperature variation can be observed (2nd, 4th, 6th and 8th point of the temperature variation curve). More specifically, these points correspond to points in the HV winding ducts, where a significant decrease in the temperature (up to 9 °C in the case of the first duct) is encountered. Fig. 12

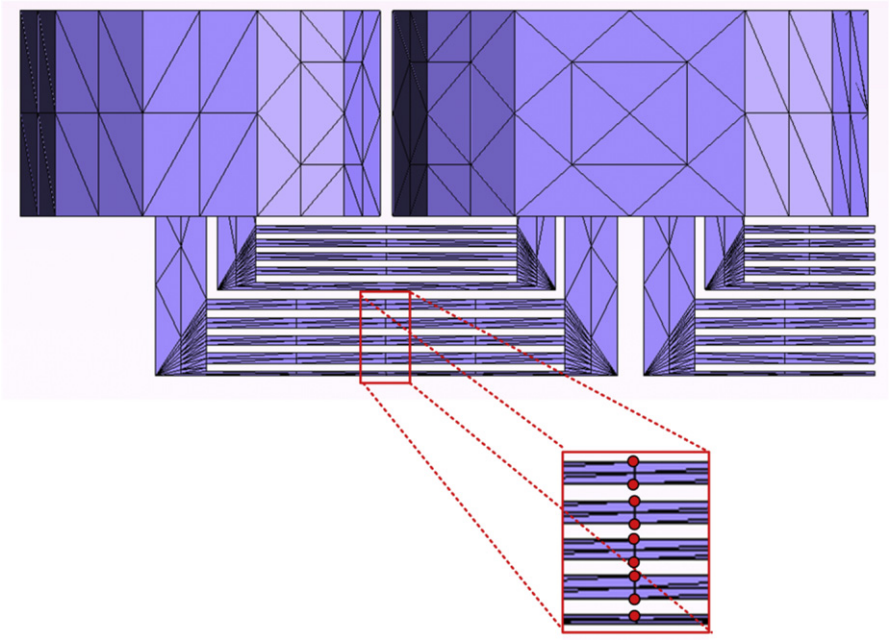

Fig. 12. Upper view of active part mesh shown in Fig. 7(a), with enlarged detail of the upper part of HV winding and the 9 nodes that correspond to the graph of Fig. 13.

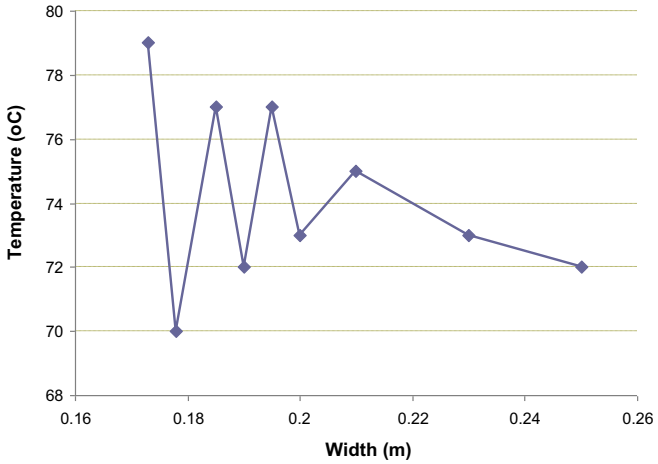

Fig. 13. Temperature variation along the middle of the HV winding face of the 400 kV A transformer (temperature of nodes illustrated in Fig. 12).

illustrates the upper view of the active part mesh, along with an enlarged detail of the upper part of HV winding with the 9 points that are contained in the graph of Fig. 13. As can be seen in this detail, due to the mesh discretization, mesh nodes are located in the middle of the HV winding (and their temperature values are used in Fig. 13) so no averaging from neighboring nodes was necessary.

Fig. 14 depicts the variation of the magnitude of the *y*-component of the oil velocity vector along the height of the winding ducts and gap. More specifically, it includes the velocity values calculated by the model at the nodes inside the ducts located at the center of the LV and HV winding and the gap between the windings. The first point of each curve corresponds to the bottom of the ducts and HV–LV gap and the last one to the upper part of the ducts and HV–LV gap. The horizontal axis of the figure reports the distance from the bottom of the tank (which is the lower boundary of the model geometry). According to Fig. 14, the values of oil velocity inside the LV and HV winding duct are quite close, while they are higher compared to the oil velocity inside the gap between the LV and HV winding, especially at their upper parts. This difference can be attributed to the fact that the heat sources inside the windings are higher, thus forcing faster oil circulation in the upper parts of the ducts area than in the respective area of the windings gap. Moreover, the width of HV–LV gap is significantly higher than the width of HV and LV ducts. The variation of oil velocity is consistent to the measured results presented in other works [30], indicating a non-linear increase up to the middle of the duct height, where the

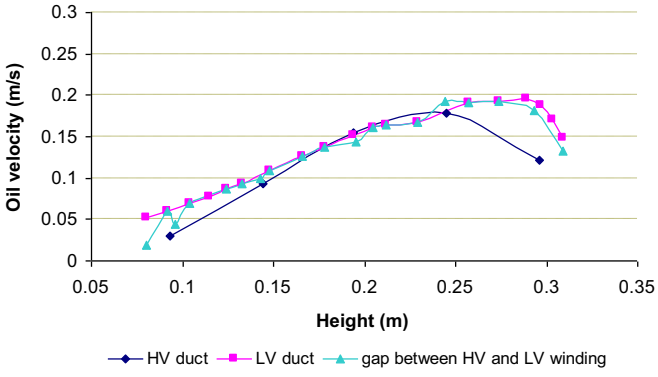

Fig. 14. Magnitude of the *y*-component of the oil velocity vector along the windings cooling ducts and gap for the 400 kV A transformer.

Table 2
Comparison of computed and measured temperatures for the 160 kV A transformer.

Point	Measured temperature (°C)	Calculated temperature (°C)	Difference (%)
Top oil	66	62	−6.1
HV winding	78.8	83.1	+5.5
LV winding	79.5	78.2	−1.6
		Quadratic average	4.8

maximum velocity is obtained, followed by a non-linear decrease along the rest of its height. It is however noted that the results presented in Ref. [16] can be used in order to obtain an overall aspect of the oil velocity variation along the transformer height and not a direct comparison of the respective oil velocity values, since they correspond to different transformer capacities, cooling system and winding configurations as well as special transformer design specifications. Detailed experimental validation by local measurements of oil velocity values inside the active part is however quite difficult and is not implemented in the present section.

3.2. Application to a 160 kV A transformer

The method was also applied to another 20/0.4 kV transformer, of rated power equal to 160 kV A and its results were compared to the available measurements. The transformer operates under nominal load, at an ambient temperature equal to 25 °C (the ambient temperature was considered equal to the respective ambient temperature during the measurement of the transformer temperature). The HV windings loss is equal to 1333 W, while the LV windings loss is equal to 1007 W. Table 2 depicts the difference between the measured and computed top oil, HV and LV winding temperatures, yielding an overall difference (quadratic average) equal to 4.8%. The top HV and LV winding temperature is measured at the center of the upper part of the winding (as depicted in Fig. 9). The top oil temperature is measured at the center of the upper part of the tank (as depicted in Fig. 8). It must be noted that although Figs. 8 and 9 refer to the 400 kV A transformer, they are also used to indicate the measurement points in the 160 kV A transformer, since the geometry configuration of the active part and tank is similar and only their dimensions are different. The deviations in the prediction of temperatures in HV winding and top oil regions are more important (5.5% and 6.1%, respectively). In counterparts, the prediction of temperature in LV windings is more accurate (less

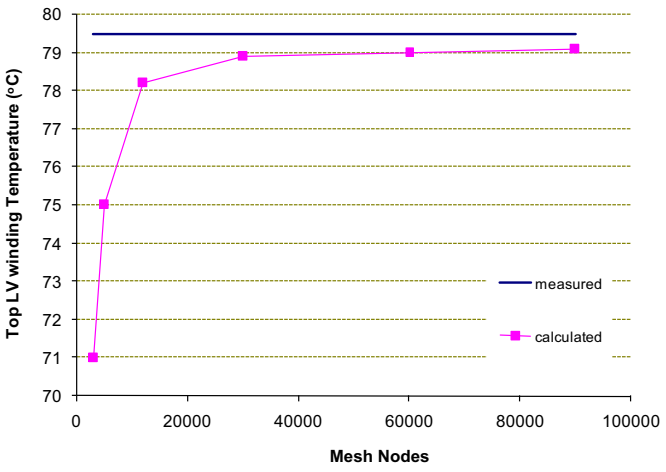

Fig. 15. Comparison of measured and calculated top LV winding temperature for the 160 kV A transformer with the use of different FEM mesh densities.

Table 3
Comparison of computed and measured top LV winding temperatures for the 160 kV A transformer with the use of different mesh densities.

Number of mesh nodes	Measured temperature (°C)	Calculated temperature (°C)	Difference (%)
3000	79.5	71.0	−10.7
5000		75.0	−5.7
12,000		78.2	−1.6
30,000		78.9	−0.8
60,000		79.0	−0.6
90,000		79.1	−0.5

Table 4
Comparison of mean execution time (at an AMD Athlon X2 Dual-Core QL-60 1.90 GHz, RAM 4 GB) of the non-linear heat and Navier–Stokes solver (for each iteration) with the use of different fem mesh densities.

Number of mesh nodes	Execution time of non-linear heat solver (min)	Execution time of non-linear Navier–Stokes solver (min)
3000	3	4
5000	5	7
12,000	9	12
30,000	15	27
60,000	30	45
90,000	60	70

than 2%) in a region with the higher temperatures, which is the most crucial for the transformer life expectancy. It is also observed that the difference for top oil temperature (Table 2) is −4 °C but for HV winding temperature it is equal to +4.3 °C. Such a large difference may explained by the approach described in Section 2.3, where the temperature T used in the material properties equations is the nodal temperature value. Therefore, the oil viscosity variation inside the ducts (where the temperature gradient is generally much higher than in other areas of the circulating oil) results to important variations of the oil velocity, partially explaining the differences between the calculated and measured values of Table 2. However, this approach is more accurate than the adoption of an average viscosity calculated over the duct length, since it provides the ability to better estimate the top winding temperature values (possibly leading to a slight overestimation which is, however, on the safe side when thermal performance is considered). The adoption of an average viscosity might lead to significantly lower temperature values in the windings and an important underestimation of the hot spot temperatures, which are more crucial than the oil temperature for transformer life expectancy. Moreover, the use of nodal temperature values provides the ability to take advantage of the mesh discretization in the ducts region and leads to more accurate results in higher mesh densities.

The above results have been obtained with the use of the optimized mesh of Fig. 7. A comparative analysis of the computational effort and accuracy of different mesh densities has also been carried out, in order to validate the sufficiency of the optimized mesh. Fig. 15 presents the comparison of measured and calculated top LV winding temperature for the 160 kV A transformer with the use of different FEM mesh densities. The data of Fig. 15 are also presented in Table 3. According to the results of Table 3, the optimized mesh of intermediate density provides sufficient accuracy, reducing significantly the deviation between the measured top LV winding temperature value and the respective calculated result yielded by the use of sparser non-optimized meshes (where the mesh is not uniform and detailed enough in the cooling ducts and tank area). The use of larger densities could further enhance the accuracy, however it would result to high execution times, as depicted in Fig. 16 and Table 4. Fig. 16 and Table 4 present the mean execution time needed for each iteration of the non-linear heat and Navier–Stokes solver, for the mesh densities of Table 3. The comparison of Tables 3 and 4 indicates that the accuracy obtained by the optimized mesh of intermediate density is sufficient, while the overall time needed for the FEM calculations is maintained within acceptable limits compared to other more dense meshes.

Fig. 17 presents the variation of the computed temperature along the inner corners of HV and LV winding (as depicted in Fig. 9). It must be noted that the maximum temperature values are obtained along the interior of the windings and not in the inner boundaries of the contours plotted in Fig. 17, thus the values of Fig. 17 are lower than the temperature values of Table 2. Fig. 18 shows the temperature variation along the middle of the HV winding face of the 160 kV A transformer, comprising the point of maximum HV winding temperature of Table 2.

It must be noted that the LV winding temperatures are lower than the ones of the HV winding temperatures (as depicted in Fig. 11 for the 400 kV A transformer and in Fig. 17, for the 160 kV A transformer). This is attributed to the fact that, in both transformers, the HV windings loss is much higher than the respective LV windings loss. More specifically, in the case of the 400 kV A transformer, the HV windings loss is equal to 1853 W, while the LV

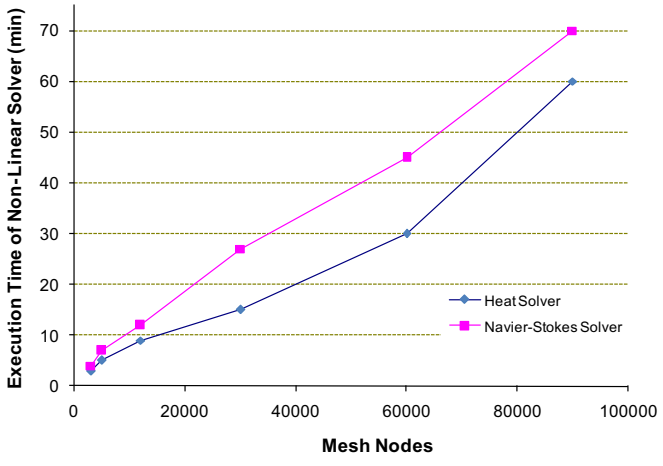

Fig. 16. Comparison of mean execution time (at an AMD Athlon X2 Dual-Core QL-60 1.90 GHz, RAM 4 GB) of the non-linear heat and Navier–Stokes solver (for each iteration) with the use of different FEM mesh densities.

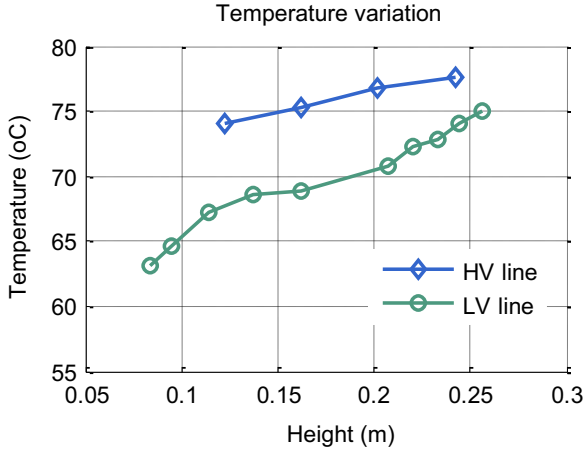

Fig. 17. Temperature variation along the inner corner of HV and LV winding of the 160 kV A transformer (as illustrated in Fig. 9).

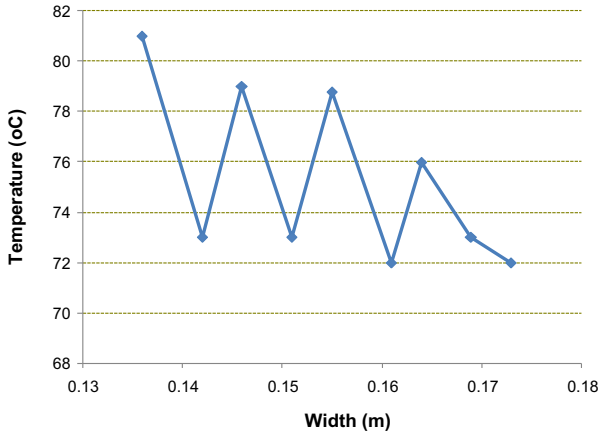

Fig. 18. Temperature variation along the middle of the HV winding face of the 160 kV A transformer (temperature of nodes illustrated in Fig. 12 – point 5 corresponds to the top HV winding temperature of Table 2).

windings loss is equal to 1554 W (as reported at the beginning of Section 3.1), while in the case of the 160 kV A transformer, the HV windings loss is equal to 1333 W, while the LV windings loss is equal to 1003 W (as reported at the beginning of Section 3.2).

4. Conclusion

In the present paper, the development of a coupled three-dimensional heat transfer and fluid flow FEM model for the prediction of ONAN transformer thermal performance was presented. The method is able to predict transformer thermal distribution without prior knowledge of thermal nodal properties, taking properly into account the effect of oil circulation. It must be noted that in case of forced cooling the implementation of turbulence models will be necessary. Further steps for the precision enhancement of the method proposed involve the adoption of proper turbulence models for the oil circulation as well as the accurate modeling of heat dissipation in transformer cores and windings and their anisotropic material properties. Moreover, the inclusion of eddy currents in steel parts is an important contribution and will be implemented in future developments of the proposed model.

References

[1] E.I. Amoiralis, M.A. Tsili, A.G. Kladas, Transformer design and optimization: a literature survey, IEEE Trans. Power Delivery 24 (4) (Oct. 2009) 1999–2024.
[2] L. Pierce, Predicting hottest spot temperatures in ventilated dry type transformer windings, IEEE Trans. Power Delivery 9 (2) (Apr. 1994) 1160–1172.
[3] E.G. teNyenhuis, R.S. Girgis, G.F. Mechler, G. Zhou, Calculation of core hot-spot temperature in power and distribution transformers, IEEE Trans. Power Delivery 17 (4) (Oct. 2002) 991–995.
[4] M.D. Hwang, W.M. Grady, H.W. Sanders, Calculation of winding temperatures in distribution transformers subjected to harmonic currents, IEEE Trans. Power Delivery 3 (3) (Jul. 1988) 1074–1079.
[5] M.B. Eteiba, M.M.A. Aziz, J.H. Shazly, Heat conduction problems in SF_6 gas cooled-insulated power transformers solved by the finite-element method, IEEE Trans. Power Delivery 23 (3) (Jul. 2008) 1457–1463.
[6] K. Preis, O. Bíró, G. Buchgraber, I. Ticar, Thermal-electromagnetic coupling in the finite-element simulation of power transformers, IEEE Trans. Magn. 42 (4) (Apr. 2006) 999–1002.
[7] C.C. Hwang, P.H. Tang, Y.H. Jiang, Thermal analysis of high-frequency transformers using finite elements coupled with temperature rise method, IEE Proc. Electr. Power Appl. 152 (4) (Jul. 2005) 832–836.
[8] A. Lefèvre, L. Miègeville, J. Fouladgar, G. Olivier, 3-D computation of transformers overheating under nonlinear loads, IEEE Trans. Magn. 41 (5) (May 2005) 1564–1567.
[9] M.A. Tsili, E.I. Amoiralis, A.G. Kladas, A.T. Souflaris, Hybrid numerical-analytical technique for power transformer thermal modeling, IEEE Trans. Magn. 45 (3) (2009) 1408–1411.
[10] C. Rosas, N. Moraga, V. Bubnovich, R. Fischer, Improvement of the cooling process of oil-immersed electrical transformers using heat pipes, IEEE Trans. Power Delivery 20 (3) (Jul. 2005) 1955–1961.
[11] E.J. Kranenborg, C.O. Olsson, B.R. Samuelsson, L.-Å. Lundin, R.M. Missing, Numerical study on mixed convection and thermal streaking in power transformer windings, in: Proceedings of the 5th European Thermal-Sciences Conference, The Netherlands (2008).
[12] J.M. Mufuta, E. van den Bulck, Modelling of the mixed convection in the windings of a disc-type power transformer, Appl. Therm. Eng. 20 (2000) 417–437.
[13] N. El Wakil, N.-C. Chereches, J. Padet, Numerical study of heat transfer and fluid flow in a power transformer, Int. J. Therm. Sci. 45 (2006) 615–626.
[14] J. Smolka, A.J. Nowak, L.C. Wrobel, Numerical modelling of thermal processes in an electrical transformer dipped into polymerised resin by using commercial CFD package fluent, Comput. Fluids 33 (2004) 859–868.
[15] C. Ortiz, A.W. Skorek, M. Lavoie, P. Bénard, Parallel CFD analysis of conjugate heat transfer in a dry-type transformer, IEEE Trans. Ind. Appl. 45 (4) (Jul. 2009) 1530–1534.
[16] J. Smolka, A.J. Nowak, Experimental validation of the coupled fluid flow, heat transfer and electromagnetic numerical model of the medium-power dry-type electrical transformer, Int. J. Therm. Sci. 7 (2008) 1393–1410.
[17] J. Smolka, D.B. Ingham, L. Elliott, A.J. Nowak, Enhanced numerical model of performance of an encapsulated three-phase transformer in laboratory environment, Appl. Therm. Eng. 27 (2007) 156–166.
[18] R. Rannacher, Finite element methods for the incompressible Navier–Stokes equations, Lecture Notes, Institute of Applied Mathematics, University of Haidelberg, August 1999.
[19] M.M. Rathore, R.R.A. Kapuno, Engineering Heat Transfer. Jones & Bartlett Learning, Massachussets, USA, 2011.
[20] S. Som, Introduction to Heat Transfer. PHI Learning Private Limited, New Delhi, 2008.
[21] E.I. Amoiralis, P.S. Georgilakis, M.A. Tsili, A.G. Kladas, Global transformer optimization method using evolutionary design and numerical field computation, IEEE Trans. Magn. 45 (3) (Mar. 2009) 1720–1723.
[22] M. Olson, Comparison of various finite element solution methods for the Navier–Stokes equations, , In: Finite Elements in Water Resources. Pentech Press, London, 1977, p. 4.185.
[23] M. ur Rehman, C. Vuik, G. Segal, A comparison of preconditioners for incompressible Navier–Stokes solvers, Int. J. Numer. Meth. Fluid. (2007) Wiley IntersScience.
[24] IEEE Guide for Loading Mineral-Oil-Immersed Transformers, IEEE Std C57.91, 2002.
[25] F. Farahmand, F.P. Dawson, J.D. Lavers, Temperature rise and free-convection heat-transfer coefficient for two-dimensional pot-core inductors and transformers, IEEE Trans. Ind. Appl. 45 (6) (Nov.–Dec. 2009) 2080–2089.
[26] E.I. Amoiralis, P.S. Georgilakis, M.A. Tsili, A.G. Kladas, A.T. Souflaris, A complete software package for transformer design optimization and economic evaluation analysis, Mater. Sci. Forum 670 (April 2011) 535–546.
[27] C. Geuzaine, J.-F. Remacle, Gmsh: a three-dimensional finite element mesh generator with built-in pre- and post-processing facilities, Int. J. Numer. Meth. Eng. 79 (11) (2009) 1309–1331.
[28] Elmer, Open Source Finite Element Software for Multiphysical Problems. http://www.csc.fi/english/pages/elmer.
[29] M.A. Tsili, E.I. Amoiralis, A.G. Kladas, A.T. Souflaris, Coupled 3D fluid flow-thermal FEM model for power transformer temperature analysis, in: Proceedings of the 17th International Conference on the Computation of Electromagnetic Fields (COMPUMAG 2009), Florianopolis, Brazil (Nov. 2009).
[30] M. Yamaguchi, T. Kumasaka, Y. Inui, S. Ono, The flow rate in a self-cooled transformer, IEEE Trans. Power Apparatus Systems PAS-100 (3) (Mar. 1981) 956–963.

Marina A. Tsili was born in Greece, in 1976. She received the Diploma in Electrical and Computer Engineering in 2001 and the Ph.D. degree in 2005 from the National Technical University of Athens, Greece. From 2005 to 2006 she worked for the Distribution Division of the Public Power Corporation of Greece, in high and medium voltage substation studies. In 2007, she joined the Hellenic Transmission System Operator as a power systems engineer. Since 2005, she is collaborating with the National Technical University of Athens as a research associate. Her research interests include transformer and electric machine modeling as well as analysis of generating units by renewable energy sources. She is a member of IEEE and the Technical Chamber of Greece.

Eleftherios I. Amoiralis was born in Greece, in 1980. He received the Diploma in Production and Management Engineering, the M.Sc. in Industrial Engineering, and the Ph.D. degree in the field of Electric Power Systems from the Technical University of Crete (TUC), Greece, in 2004, 2005, and 2008, respectively. From 2010 to present, he is an Assistant Professor in the Technological Educational Institute of Chalkida, Greece (Department of Electrical Engineers). From 2005 to 2009, he was occupied in Schneider Electric AE as a freelancer. Since 2008 he is collaborating with the Technical University of Crete as a research associate. His current research interests include transformer cost evaluation, energy-efficient transformers, transformer design optimization, electric machines modeling as well as artificial intelligence. Dr. Amoiralis is

member of the Technical Chamber of Greece since 2005 as well as Member of the IEEE since 2009.

Antonios G. Kladas was born in Greece, in 1959. He received the Diploma in Electrical Engineering from the Aristotle University of Thessaloniki, Greece in 1982 and the DEA and Ph.D. degrees in 1983 and 1987, respectively from the University of Pierre and Marie Curie (Paris 6), France. He served as Associate Assistant in the University of Pierre and Marie Curie from 1984 to 1989. During the period 1991–1996 he joined the Public Power Corporation of Greece, where he was engaged in the System Studies Department. Since 1996 he joined the Department of Electrical and Computer Engineering of the National Technical University of Athens (NTUA), where he is now Professor. His research interests include transformer and electric machine modeling and design as well as analysis of generating units by renewable energy sources and industrial drives.

Athanassios T. Souflaris was born in Athens, Greece in 1956. He received the Diploma in Electrical Engineering from the Technical University of Pireaus, Greece in 1981. He joined Schneider Electric AE in 1985 as Transformer Design Engineer and from 1988 he is the Transformer Design Manager of Schneider Electric AE.